



# 3D-hierarchically structured MnO<sub>2</sub> for catalytic oxidation of phenol solutions by activation of peroxydisulfate: Structure dependence and mechanism

Yuxian Wang, Hongqi Sun\*, Ha Ming Ang, Moses O. Tadé, Shaobin Wang\*

Department of Chemical Engineering and CRC for Contamination Assessment and Remediation of the Environment (CRC CARE), Curtin University, GPO Box U1987, WA 6845, Australia

## ARTICLE INFO

### Article history:

Received 4 June 2014

Received in revised form 17 August 2014

Accepted 4 September 2014

Available online 16 September 2014

### Keywords:

Manganese oxide

Oxone

Oxidation

Hierarchical material

Phenol

## ABSTRACT

Hierarchical materials have facilitated fascinating applications in heterogeneous catalysis due to that micro-sized bulk is easily separable and nano-sized sub-blocks can significantly enhance catalytic performance. In this study, corolla-like  $\delta$ -MnO<sub>2</sub> with sub-blocks of nanosheets, and urchin-shaped  $\alpha$ -MnO<sub>2</sub> with sub-blocks of nanorods were synthesized by a simple hydrothermal route. The hydrothermal temperature significantly influenced the crystal structure, morphology and textural structure of the obtained three-dimensional (3D) MnO<sub>2</sub> catalysts. The catalytic activities of three samples prepared at 60, 100 and 110 °C (denoted as Mn-60, -100 and -110, respectively) were thoroughly evaluated by activation of peroxydisulfate (PMS) for catalytic oxidation of phenol solutions. Based on first-order kinetics, the rate constants of Mn-60, -100 and -110 catalysts were determined to be 0.062, 0.132, and 0.075 min<sup>-1</sup>, respectively. The activation energy of Mn-100 in catalytic oxidation of phenol solutions was estimated to be 25.3 kJ/mol. The catalytic stability of Mn-100 was also tested and discussed by monitoring Mn leaching. Electron paramagnetic resonance (EPR), quenching tests, total organic carbon (TOC) analysis and identification of intermediates were applied to illustrate the activation processes of PMS and the mechanism of phenol degradation.

© 2014 Elsevier B.V. All rights reserved.

## 1. Introduction

Aqueous organic pollutants, discharged from natural processes, industrial activities, and households, are detrimental to human health and eco-environment. As one of the important organic pollutants in wastewater, phenol is widely used in many industrial processes, such as chemical, petrochemical and pharmaceutical industries [1]. Moreover, phenol and phenolic compounds are not only resistant to natural degradation, but toxic even at a low concentration, therefore development of effective strategies for removal of phenolics from water are highly in demand [2,3]. In the past a few years, advanced oxidation processes (AOPs) have been widely applied owing to the promising capability of complete decomposition of the organics. As one of typical AOPs, Fenton reaction has demonstrated to be highly effective in complete removal of pollutants by producing hydroxyl radicals ( $\cdot$ OH) [4]. To overcome

the limitations of Fenton reaction, such as low pH 3–4, large amount of sludge produced and metal leaching, sulfate radicals were introduced as an alternative to hydroxyl radicals [5–7]. Sulfate radicals can be effectively activated in both homogeneous [8,9] and heterogeneous cobalt catalysis [10,11], metal leaching problem leading to secondary contamination can thus be minimized. However, for cobalt catalysis, neither homogeneous nor heterogeneous reactions can completely prevent the cobalt leaching, which might lead to severe health problems [12–14]. Therefore, sourcing novel catalysts for activation of PMS is critical in employment of sulfate radicals for environmental remediation.

Manganese oxides are common metal oxides present in soils and have a low toxicity to the environment. As promising catalysts alternative to Fe-based materials, a variety of Mn oxides were applied in Fenton or Fenton-like reactions for producing hydroxyl radicals [15,16]. In a recent study on supported cobalt catalysts, we for the first time discovered that  $\alpha$ -MnO<sub>2</sub> has a moderate activity in activation of PMS [17]. Thereafter, several  $\alpha$ -MnO<sub>2</sub> catalysts in forms of nanospheres, nanorods and nanowires were developed and used in activation of PMS. Crystalline phase of the materials was found to play a critical role in the catalytic oxidation of phenol [18].

\* Corresponding authors.

E-mail addresses: [h.sun@curtin.edu.au](mailto:h.sun@curtin.edu.au) (H. Sun), [shaobin.wang@curtin.edu.au](mailto:shaobin.wang@curtin.edu.au), [wangshao@vesta.curtin.edu.au](mailto:wangshao@vesta.curtin.edu.au) (S. Wang).

The effects of oxidation states of manganese on activation of PMS were also investigated by employing a series of  $\text{MnO}_x$  ( $\text{MnO}$ ,  $\text{MnO}_2$ ,  $\text{Mn}_2\text{O}_3$  and  $\text{Mn}_3\text{O}_4$ ). It was suggested that the activity follows an order of  $\text{Mn}_2\text{O}_3 > \text{MnO} > \text{Mn}_3\text{O}_4 > \text{MnO}_2$  [19]. Shape-controlled synthesis can significantly improve the catalytic activity of the oxides, owing to the intrinsic atomic arrangements of the exposed facets [20].  $\text{Mn}_2\text{O}_3$  shaped in cube, octahedra and truncated octahedra showed different activities in phenol degradation, with the highest phenol oxidation achieved on cubic  $\text{Mn}_2\text{O}_3$  [21].  $\alpha$ -,  $\beta$ - and  $\gamma$ - $\text{MnO}_2$  materials presented in morphologies of nanowires, nanorods and nanofibers respectively were examined in catalytic oxidation of phenol, and  $\alpha$ - $\text{MnO}_2$  showed the highest activity [22]. So far, hierarchically structured Mn oxides have not been employed for activation of PMS in environmental applications. Moreover, the PMS activation processes have not been well illustrated.

Three-dimensional (3D) structures are of much importance because of their attractive physical and chemical properties [23–25]. It would be very interesting to apply hierarchical materials in heterogeneous catalysis because they can both remain easy separation of bulk materials and provide a high performance due to the nanostructure. The successful synthesis of 3D manganese oxides has been reported recently. Li et al. [26] reported a homogeneous catalytic route to prepare urchin-like sphere network and nanowire network of  $\alpha$ - $\text{MnO}_2$  hierarchical nanostructures. Yu et al. [27] reported 3D sea-urchin like and 3D clew-like  $\text{MnO}_2$  by a hydrothermal method using  $\text{MnSO}_4$  and  $\text{K}_2\text{S}_2\text{O}_8$  as precursors and tested their performance as electrochemical supercapacitors. Duan et al. [28] synthesized 3D nanocube-like  $\text{MnO}_2$  by using  $\text{KMnO}_4$ ,  $\text{Mn}(\text{AC})_2 \cdot 4\text{H}_2\text{O}$  and glucose as precursors and poly(vinylpyrrolidone) as a surfactant.

In this study, we demonstrated a facile one-pot hydrothermal method to synthesize corolla and sea-urchin shaped  $\text{MnO}_2$  nanostructures by reduction of potassium permanganate solution under hydrochloric acid condition without any surfactant.  $\text{MnO}_2$  in 3D hierarchical structures were selectively obtained by simply varying the reaction temperature in the hydrothermal process and showed microscale in diameter and nanoscale in sub-blocks of nanosheets or nanorods. The prepared catalysts showed outstanding catalytic activity in activation of PMS for degradation of phenol solutions and remarkable stability for repeating uses. The PMS activation processes and the mechanism of catalytic oxidation of phenol on  $\text{MnO}_2$  were further investigated by means of EPR studies.

## 2. Experimental

### 2.1. Materials

Potassium permanganate (99.8%), hydrochloric acid (37%), and phenol (99%), ethanol (99.9%) and tert-butyl alcohol (99.9%) were purchased from Sigma–Aldrich. Oxone® ( $2\text{KHSO}_5 \cdot \text{KHSO}_4 \cdot \text{K}_2\text{SO}_4$ , PMS) was obtained from Aldrich. 5,5-Dimethyl-1-pyrroline (DMPO, >99.0%) and commercial activated Mn (IV) dioxide (99.9%) were obtained from Fluka. All chemicals were used as received without further purification.

### 2.2. Synthesis of hierarchically structured $\text{MnO}_2$

3D-hierarchically structured  $\text{MnO}_2$  was prepared by a modified hydrothermal process with reduction of  $\text{KMnO}_4$  reported by Xiao et al. [29]. The concentration of precursors and hydrothermal temperatures were modified to obtain desired nanostructured  $\text{MnO}_2$  materials. Scheme 1 shows the preparation procedure of  $\text{MnO}_2$  catalysts. In a typical synthesis, 2.8 mmol (0.45 g) of  $\text{KMnO}_4$  was first dissolved in 80 mL of deionized water. Then 0.027 mol of HCl (37 wt%) was added to the solution drop wisely under magnetic



Scheme 1. Synthesis procedure of  $\text{MnO}_2$  nanostructures.

stirring to form the precursor solution. After stirring for about 20 min, the solution was transferred into a Teflon-lined stainless steel autoclave with the capacity of 120 mL. The autoclave was then heated in an electric oven at 60, 100 and 110 °C for 12 h, respectively. After the autoclave was naturally cooled down to room temperature, each of the black precipitate was harvested by vacuum filtration and washed with deionized water for 3 times before being dried at 60 °C overnight. Referring to the hydrothermal temperature, the obtained samples were labelled as Mn-60, -100 and -110, respectively.

### 2.3. Characterization

The structure and morphology of the materials were observed on a ZEISS NEON 40EsB scanning electron microscope (SEM). XRD (X-ray diffraction) patterns were obtained on a Bruker D8 diffractometer (Bruker-AXS, Karlsruhe, Germany) using filtered  $\text{Cu K}\alpha$  radiation ( $\lambda = 1.5418 \text{ \AA}$ ) with an accelerating voltage of 40 kV and a current of 30 mA. The Brunauer–Emmett–Teller (BET) specific surface area and the pore size distribution of the samples were evaluated by  $\text{N}_2$  adsorption/desorption using a Micromeritics Tristar 3000. Prior to measurement the samples were degassed at 100 °C overnight under vacuum condition.

### 2.4. PMS activation and catalytic oxidation

The catalytic oxidation of phenol was carried out in a 500 mL reactor containing 20 mg/L of phenol solution with a constant stirring at 400 rpm. The reactor was attached to a stand and dipped into a water bath with a temperature controller. Unless specifically stated, the reaction temperature was 25 °C. In a typical test, firstly, 0.1 g catalyst was added into the phenol solution for 30 min to achieve adsorption–desorption equilibrium, then Oxone® was added into the solution at 2 g/L. At certain intervals, 1 mL aqueous sample was withdrawn by a syringe and filtered into a HPLC vial, which was prior injected by 0.5 mL of methanol to quench the reaction. For catalytic phenol degradation, each experiment was repeated in order to obtain error bars on the plots. The concentration of phenol was analyzed using a Varian HPLC with a UV detector at wavelength of 270 nm. A C-18 column was used to separate the organics while the mobile phase with a flow rate of 1 mL/min was made of 30%  $\text{CH}_3\text{CN}$  and 70% water.

Total organic carbon (TOC) was determined using a Shimadzu TOC-5000 CE analyzer for selected samples. For the measurement of TOC, 10 mL sample was extracted at a fixed interval and quenched with 10 mL of 0.3 M sodium nitrite solution and then analyzed [7]. The intermediates of phenol degradation were investigated by HPLC. Classical quenching tests were performed on corolla-like  $\text{MnO}_2$  (Mn-100) using ethanol (EtOH) and tert-butyl alcohol (TBA) as quenching agents to distinguish the dominant reactive species for phenol degradation.

For the recycle tests of the catalyst, the material was obtained by vacuum filtration and washed with ultrapure water for several times after each run. Then the washed catalyst was dried in

an oven at 60 °C for 12 h. For radical detection, various electron paramagnetic resonance (EPR) experiments were performed on a Bruker EMX-E spectrometer (Germany) with DMPO as a spin-trapping agent.

### 3. Results and discussion

#### 3.1. Characterization of the hierarchical materials

Fig. 1 shows XRD patterns of three MnO<sub>2</sub> nanostructures. Mn-60 and Mn-100 display similar XRD patterns. Diffraction peaks at 12.3, 25.5, 36.7 and 66.2° were observed, corresponding to the crystal planes of (001), (002), (111) and (311), respectively. The XRD patterns of Mn-60 and Mn-100 were identified to the pure layered birnessite-type MnO<sub>2</sub> (JCPDS No. 80-1098, monoclinic, *C2/m*, *a* = 5.15 Å, *b* = 2.84 Å, *c* = 7.17 Å), denoted as δ-MnO<sub>2</sub> [29]. While the pattern of Mn-110 confirmed the formation of α-MnO<sub>2</sub> (JCPDS No. 44-0141, tetragonal, *I4/m*, *a* = *b* = 9.78 Å, *c* = 2.86 Å) [27]. The characteristic peaks in Mn-60 pattern were much broader than those of Mn-100, indicating that the crystallinity of Mn-60 sample was not as high as Mn-100. As seen, at hydrothermal temperature below 100 °C, the crystal structures of the synthesized samples were similar, while crystalline structure would be changed at the temperature above 100 °C. Moreover, since no other characteristic peaks were observed, the obtained samples were confirmed to be of high purity.

The reactions involved in the hydrothermal process for MnO<sub>2</sub> formation can be briefly described as follows [26].

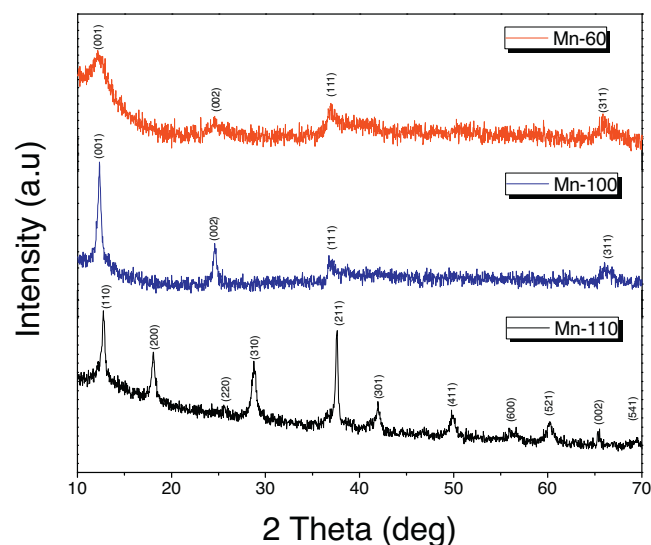
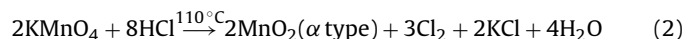
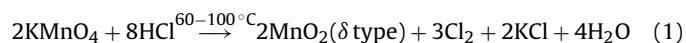


Fig. 1. XRD patterns of Mn-60, -100 (δ-MnO<sub>2</sub>) and -110 (α-MnO<sub>2</sub>).

Fig. 2 shows SEM images of the synthesized samples for displaying their structure and morphology. Fig. 2(A) and (B) illustrates SEM images of Mn-60. It can be observed that this product is presented as uniform δ-MnO<sub>2</sub> nanosphere with an average diameter of 200 nm, which is consisted of developing nanosheets on the surface. The SEM images of Mn-100 are shown in Fig. 2(C) and (D). The microsphere/nanosheet hierarchical nanostructures with a diameter of 2–3 μm were observed. Compared with Mn-60, the nanosheets on Mn-100 surface grew more compact and deeper, and thus providing

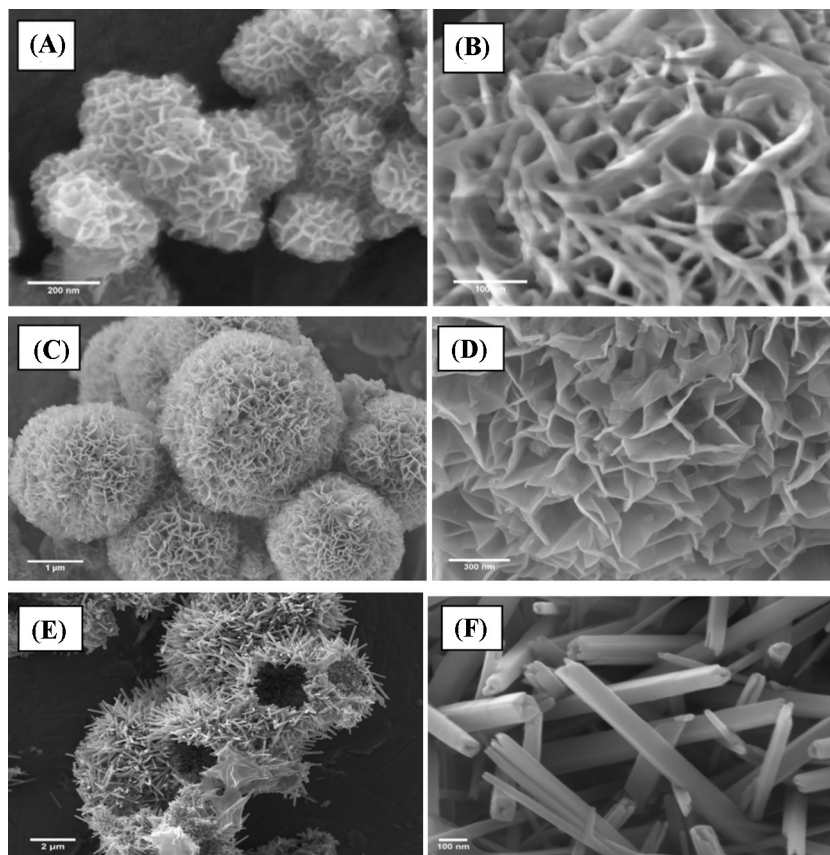


Fig. 2. SEM images of Mn-60 (A and B), -100 (C and D) and -110 (E and F).

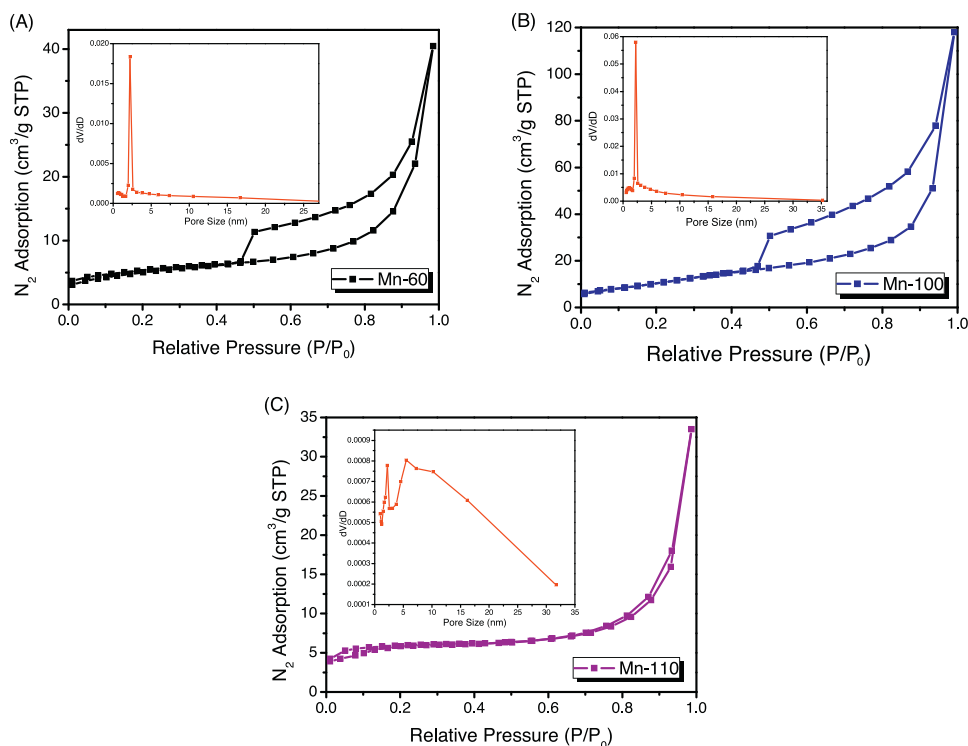


Fig. 3. Nitrogen sorption isotherms and pore size distribution of Mn-60 (A), -100 (B) and -110 (C).

a larger diameter with more corolla-like morphology. The growth of the nanosheets is significantly affected by the hydrothermal temperature (60–100 °C), and the nanosheets on the  $MnO_2$  nuclei gradually develop and grow up perpendicular to the  $MnO_2$  nuclei. The growth mechanism from  $MnO_2$  nuclei to corolla-like microspheres can be ascribed as follows. In the first phase, preliminary crystallization process occurred. A large number of nuclei were formed within a rather short time period. With the aid of pressure and temperature, the nuclei would develop larger. Meanwhile, the heterogeneous growth of 2D nanosheets on these nuclei happened and the diameter of the nanoparticles as well as the compactness of the 2D nanosheets within the corolla were strongly dependent on the precursors' concentrations [30].

When hydrothermal temperature was further increased to 110 °C, corolla-like microspheres consisting of 2D nanosheets converted to hollow sea-urchin shaped  $MnO_2$  with a diameter of 3–4  $\mu m$  (Fig. 2(E) and (F)). The hollow sea-urchin shaped  $MnO_2$  particles are made of straight hollow tetragonal nanorods with a uniform diameter of 30–40 nm. Comparison of the three samples suggested that  $MnO_2$  experienced a phase change at around 100–110 °C in current synthesis route, as also confirmed by XRD patterns.

Fig. 3 shows  $N_2$  adsorption/desorption isotherms and the associated pore size distribution of three  $MnO_2$  samples. It can be seen that all the three samples possess the type IV isotherm with a type H3 hysteresis loop indicating a mesoporous structure [31]. Comparison of the specific surface area and pore size distribution was shown in Table 1. It was found that Mn-100 presents the highest surface area of 41.7  $m^2/g$  and a large pore volume of 0.149  $cm^3/g$ . While Mn-60 and Mn-110 show the similar surface area (19.4 and 17.5  $m^2/g$ , respectively). The difference in surface areas of the samples was also reflected by SEM images shown previously. The highest surface area and pore volume of Mn-100 were attributed to the compact and deep 2D nanosheets. While the scattered and shallow layer of Mn-60 sample and urchin-like structure of Mn-110 would not contribute much to either surface area or pore volume.

The hysteresis loops of Mn-60 and Mn-100 samples are similar, and are broad in a lower relative pressure range ( $0.45 < P/P_0 < 0.9$ ). Moreover, both samples have a rather narrow pore size distribution concentrating at a similar position around 2.5 nm and thus resulting in a similar average pore size (6.7 nm for Mn-60 and 6.3 nm for Mn-100).

Comparatively, sea-urchin-like sample (Mn-110) demonstrated a narrow hysteresis loop at a relative pressure ( $P/P_0$ ) range of 0.6–0.95 and a bimodal pore size distribution concentrating at 2.2 and 6.3 nm, respectively (Fig. 3(C)). Based on the SEM image shown in Fig. 2(F), the occurrence of the bimodal pore distribution can be ascribed to the hollow structure of the tetragonal nanorods and the void space enclosed by the tetragonal nanorods. Moreover, due to the hollow structure and the void space, the average pore size of Mn-110 was almost double as compared to that of Mn-60 and Mn-100.

### 3.2. Catalytic oxidation of phenol

Fig. 4 presents phenol removal profiles under various reaction conditions. In order to provide benchmark for the catalytic performance of  $MnO_2$ , control experiments were carried out to investigate PMS self-oxidation and catalyst self-adsorption. It was found that without  $MnO_2$  as the catalyst, PMS could not induce significant phenol degradation. Less than 4% of phenol was degraded after 120 min, indicating that, at current experimental conditions, thermal activation of PMS for production of reactive sulfate radicals is negligible. For adsorption on various  $MnO_2$  nanostructures without PMS, similar trend was observed and less than 5% of phenol was adsorbed in 120 min. Corolla-like  $MnO_2$  (Mn-100) presented a higher adsorption than others due to the higher BET surface area and larger pore volume. The fluctuation of phenol removal profiles in the first 30 min can be ascribed to achieving adsorption/desorption equilibrium. For catalytic reactions with the presence of PMS, all the three  $MnO_2$  nanostructures demonstrated superior catalytic activity to the commercial activated  $MnO_2$  which



**Table 1**Textural property of MnO<sub>2</sub> catalysts and their activities in phenol degradation.

Catalyst	Surface area ( $S_{\text{BET}}$ m <sup>2</sup> /g)	Pore volume (cm <sup>3</sup> /g)	Average pore diameter (nm)	First-order rate constant (min <sup>-1</sup> )	$R^2$
Mn-60	19.4	0.0493	6.7	0.059	0.992
Mn-100	41.7	0.149	6.3	0.19	0.993
Mn-110	17.5	0.0412	11.6	0.069	0.999

provided a less than 20% phenol degradation after 120 min. Corolla-like Mn-100 showed the highest activity for activation of PMS to produce sulfate radicals and 100% phenol removal was achieved within 30 min. Sea-urchin like MnO<sub>2</sub> (Mn-110) possessed a lower activity and provided 100% phenol removal in 45 min. While Mn-60 presented the least phenol degradation rate and 100% phenol removal was achieved after 60 min.

Previous researches have shown that Co and Mn based catalytic reactions for phenol degradation using PMS as an oxidant followed a first-order kinetic model [17,21,32–34]. In this study, a first-order kinetic model (Eq. (3)) was applied for evaluation of the kinetics of phenol degradation.

$$\ln \left( \frac{C}{C_0} \right) = -kt \quad (3)$$

where  $C$  and  $C_0$  are the phenol concentrations at time ( $t$ ) and  $t=0$ , respectively and  $k$  is the reaction rate constant. Fig. 5 shows that

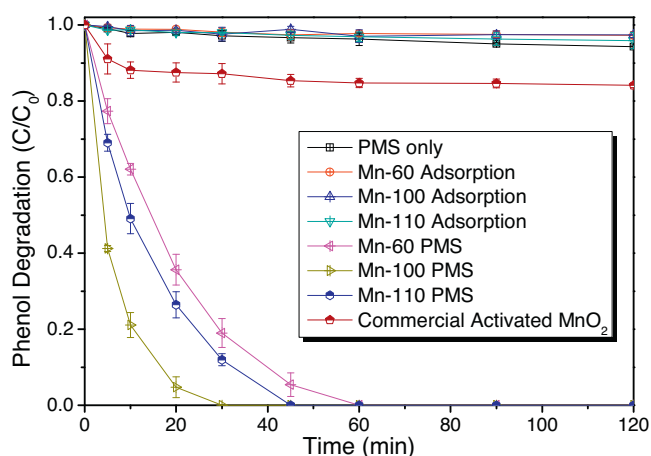


**Fig. 4.** Phenol removal on different materials in adsorption and reaction. Reaction conditions: [phenol]<sub>0</sub> = 20 mg/L; catalyst loading = 0.2 g/L; Oxone® loading = 2.0 g/L; temperature: 25 °C.

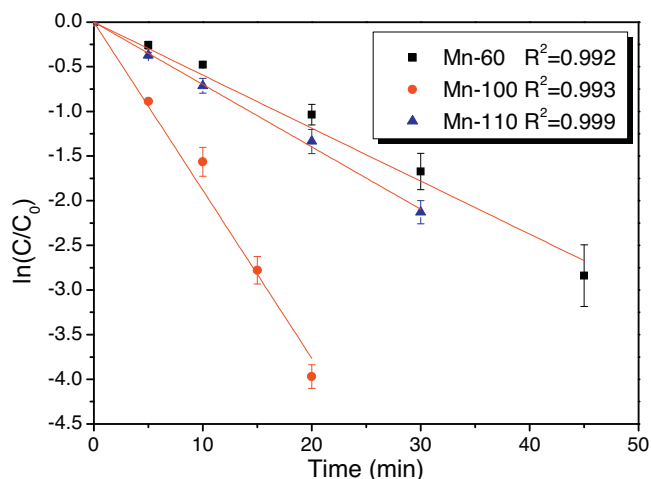


**Fig. 5.** First order kinetic model of catalytic phenol reactions.

phenol degradation curves of three MnO<sub>2</sub> nanostructures can be fitted well by the first-order kinetics with high values of regressions coefficients ( $R^2 > 0.992$ ). The reaction rate constants for the three catalysts were provided in Table 1. As seen, the reaction rate constant of corolla-like MnO<sub>2</sub> (Mn-100) was about 3 times higher than Mn-60.

It was evidenced that MnO<sub>2</sub> nanostructures in various shapes showed different catalytic performances in phenol degradation, and the catalytic activity of corolla-like  $\delta$ -MnO<sub>2</sub> is higher than sea-urchin like  $\alpha$ -MnO<sub>2</sub>. It was also deduced that the high catalytic activity of corolla-like  $\delta$ -MnO<sub>2</sub> can be ascribed to the higher surface area and the highly active surface facet with the arrangement of inherent distinction of surface atoms [20,21]. The shape-dependent catalytic performances of manganese oxides were also reported in other catalyst systems. Fang et al. [35] prepared  $K_x\text{MnO}_2$  nanostructures with two different morphologies (honeycomb and hollow needle), and evaluated their catalytic activity in oxidative decomposition of formaldehyde and found that honeycomb  $K_x\text{MnO}_2$  showed a superior catalytic activity to hollow needle  $K_x\text{MnO}_2$ . Zhang et al. [31] investigated shape-controlled Mn<sub>3</sub>O<sub>4</sub> nanocrystals and their catalysis for degradation of methylene blue, and found that octahedral shaped Mn<sub>3</sub>O<sub>4</sub> exposing the facet of (1 1 1) possessed an excellent catalytic activity for H<sub>2</sub>O<sub>2</sub> activation.

Fig. 6 reveals the effect of reaction temperature on phenol degradation using corolla-like MnO<sub>2</sub> (Mn-100) as the catalyst. A general trend can be observed that higher temperature will result in an increase in reaction rate. As seen, phenol degradation could reach 100% at 20 min when temperature was elevated to 35 °C. While at 25 °C, phenol was able to be fully removed in 30 min. The relationship between reaction rate and temperature reveals that the PMS activation process is an endothermic reaction: higher temperature would drive the reaction to produce more reactive sulfate and hydroxyl radicals and thus enhance the phenol degradation efficiency. To evaluate the activation energy, reaction rate constants at varying temperature were determined on the basis of the first-order kinetics and the correlation between the rate constants and

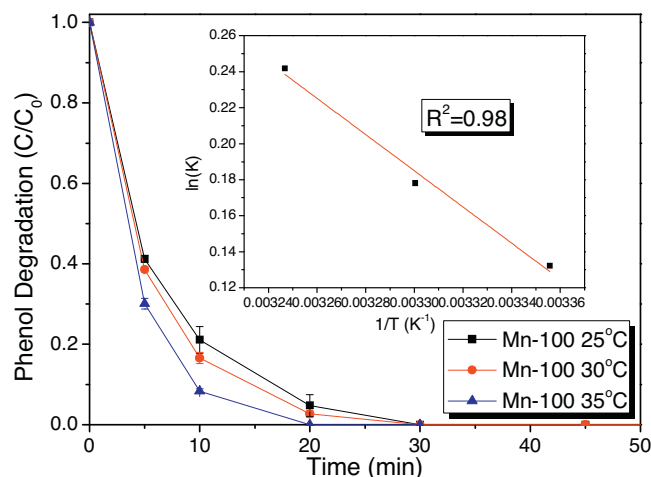


**Fig. 6.** Effect of reaction temperature on phenol degradation and estimation of activation energy. Reaction conditions: [phenol]<sub>0</sub> = 20 mg/L; catalyst loading = 0.2 g/L; Oxone® loading = 2.0 g/L.

**Table 2**  
Comparison of activation energy in Mn-based catalysis.

Catalyst	Organics	Activation energy (kJ/mol)	Reference
Mn <sub>2</sub> O <sub>3</sub> sphere	Phenol	11.4	[19]
Mn <sub>2</sub> O <sub>3</sub> cube	Phenol	61.2	[21]
α-MnO <sub>2</sub> nanowire	Phenol	21.9	[22]
Mn <sub>3</sub> O <sub>4</sub> -rGO	Orange II	49.5	[36]
Corolla-like δ-MnO <sub>2</sub>	Phenol	25.3	This work

reaction temperature was fitted by the Arrhenius equation. The relationship was shown in the inset of Fig. 6. The activation energy of Mn-100 catalytic reaction was then obtained to be 25.3 kJ/mol.

For Mn activation of PMS for organics degradation, a few of investigations have reported the kinetics and activation energies. For comparison, Table 2 summarizes the activation energies obtained from previous researches on PMS activation using Mn-based materials. As seen, corolla-like δ-MnO<sub>2</sub> presented lower activation energy than most of manganese oxide catalysts.

Fig. 7 shows the activity of recycled corolla-like δ-MnO<sub>2</sub> (Mn-100) by simple water washing in phenol degradation. As can be seen, corolla-like δ-MnO<sub>2</sub> shows a slight decrease in the second run but 100% phenol removal was still obtained within 45 min. While in the third run, the catalyst presented a similar activity as the second run, suggesting the high stability of corolla-like δ-MnO<sub>2</sub>. After each of 3 h reaction, the reaction solutions were collected and the concentrations of leached Mn ions were analyzed by atomic absorption spectroscopy (AAS SpectrAA 110, Varian). The concentration of Mn remained in the solution was detected to be around 3 ppm, which suggests the loss of catalyst activity caused by Mn leaching is negligible. The activity decrease for the second run could be attributed to the adsorption of reaction intermediates on the catalyst surface. By comparison of the reaction rates of the second and third run, it can be seen that these reaction intermediates attached on catalyst surface cannot be removed by the simple water washing process. In a recent study of phenol degradation on Mn<sub>2</sub>O<sub>3</sub>, phenol degradation decreased from 100% to 27%, but could be recovered to be almost 100% after a heat treatment of Mn<sub>2</sub>O<sub>3</sub> at 500 °C for 1 h [19]. The study strongly suggested that these intermediates can be completely removed by calcination either in air or N<sub>2</sub> atmosphere [32,37].

Fig. 8(A) presents the TOC removal profiles of phenol decomposition on various 3D MnO<sub>2</sub> catalysts. All three catalysts were able to provide efficient TOC reduction in a short time. Mn-100 provided the best TOC reduction and more than 80% of TOC was removed and

transferred into inorganic carbon forms within 45 min. While for Mn-60, around 70% of TOC was reduced after 45 min. The order of the TOC removal rates were in accordance with the order of phenol degradation rates on the various catalysts.

In order to investigate the reaction intermediates, the reaction solutions at certain intervals were analyzed using HPLC with a UV detector set at wavelength of 270 nm and the mobile phase flow rate of 0.2 mL/min. It was found that *p*-benzoquinone, 4-hydroxybenzoic acid and 1,2-dihydroxybenzene were the major intermediates during the catalytic phenol degradation reaction. The concentration variations of the intermediates with time on Mn-100 are shown in Fig. 8(B). As seen, compared with the concentration variation of 1,2-dihydroxybenzene, *p*-benzoquinone and 4-hydroxybenzoic acid were the more abundant aromatic intermediates, suggesting that hydroxylation took place predominantly in the para position [17].

### 3.3. PMS activation processes on MnO<sub>2</sub>

In activation of PMS using metal-based catalysts, it is well accepted that sulfate radicals (SO<sub>4</sub><sup>•−</sup>) are the key active species for degradation of organic pollutants [32,34,37,38]. In order to investigate the catalytic oxidation mechanism and identify whether other radicals have been involved in the reactions, EPR tests were carried out using corolla-like δ-MnO<sub>2</sub> as the catalyst and DMPO as the spin trapping agent.

As shown in Fig. 9(A), no peaks were identified in the EPR spectra when 2 g/L PMS solution was tested without adding the spin trapping agent (DMPO) or phenol solution, indicating that no spins had been trapped without DMPO. When DMPO was added in the as-mentioned PMS solution, characteristic signals with an intensity ratio of 1:2:1:2:1:2:1 were captured, which were assigned to nitroxide radicals of DMPO (5,5-dimethylpyrroline-(2)-oxyl-(1); DMPOX) [39]. The appearance of a nitroxide radical peak such as DMPOX was not derived from spin-trapping of DMPO-•OH, but from direct oxidation by single electron sources [40]. In this case, immense amount of •OH generated by H<sub>2</sub>O<sub>2</sub>, which was the hydrolysis product of HSO<sub>5</sub><sup>−</sup> and would oxidize most of the spin trapping agent to DMPOX in the absence of degradation target, phenol. And the correspondent hydrolysis reaction of HSO<sub>5</sub><sup>−</sup> is shown in Eq. (4).



When corolla-like δ-MnO<sub>2</sub> was added together with PMS (2 g/L) and phenol solution (20 mg/L), sulfate radicals and hydroxyl radicals were identified, as shown in Fig. 9(B). At 1 min, characteristic signals of DMPO-•OH adducts (with hyperfine splitting constants of  $a_N = a_H = 14.9$  G) and DMPO-SO<sub>4</sub><sup>•−</sup> adducts (with hyperfine splitting constants of  $a_N = 13.2$  G,  $a_H = 9.6$  G,  $a_H = 1.48$  G and  $a_H = 0.78$  G) were observed [32]. The appearance of DMPO-•OH and DMPO-SO<sub>4</sub><sup>•−</sup> adducts revealed that both •OH and SO<sub>4</sub><sup>•−</sup> radicals were generated at the initial phase of the reaction. In addition, no characteristic peaks of DMPOX were observed in this EPR spectrum, suggesting that with the participation of phenol, •OH preferred reacting with phenol other than DMPO.

When reaction time was prolonged to 5 min, the peak intensities of DMPO-SO<sub>4</sub><sup>•−</sup> adducts decreased dramatically. Furthermore, little or no intensities of DMPO-SO<sub>4</sub><sup>•−</sup> signals could be observed when reaction time was extended to 10 min. While within the same reaction time period (5–10 min), the peak intensities of DMPO-•OH adducts also experienced a decrease though not as sharp as DMPO-SO<sub>4</sub><sup>•−</sup> adducts. And in the EPR spectra at 10 min, only signals of DMPO-•OH adducts were identified. The sharper intensity decrease of DMPO-SO<sub>4</sub><sup>•−</sup> adducts indicates that sulfate radicals were more active than hydroxyl radicals in phenol degradation process. The rapid intensity decrease of the radicals is also in agreement with the fast reaction rate of corolla-like δ-MnO<sub>2</sub> shown in Table 1.

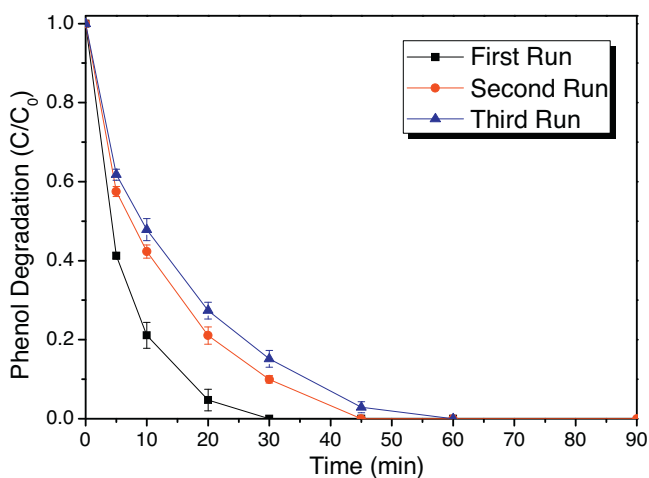


**Fig. 7.** Phenol degradation on Mn-100 at different runs after repeated uses. Reaction conditions: [phenol]<sub>0</sub> = 20 mg/L; catalyst loading = 0.2 g/L; Oxone<sup>®</sup> loading = 2.0 g/L; and *T* = 25 °C.

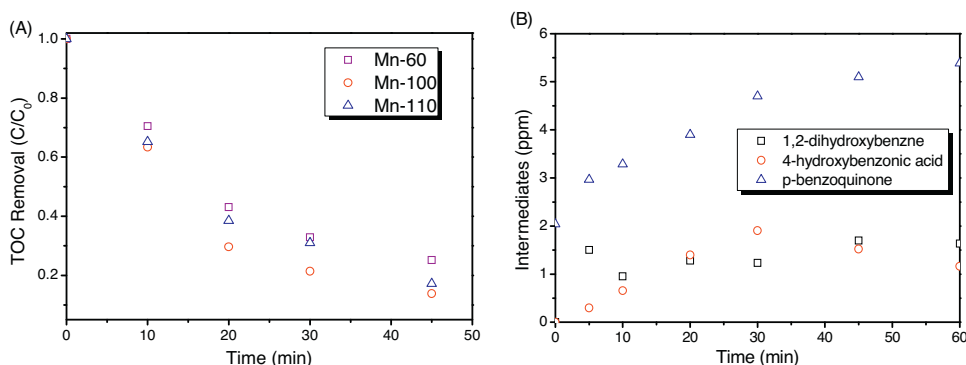


**Fig. 8.** TOC removal profiles and variation of intermediate concentrations during phenol degradation. (A) TOC removal efficiencies during phenol degradation on various 3D MnO<sub>2</sub> catalysts. (B) Variation of intermediate concentrations during phenol degradation on Mn-100.

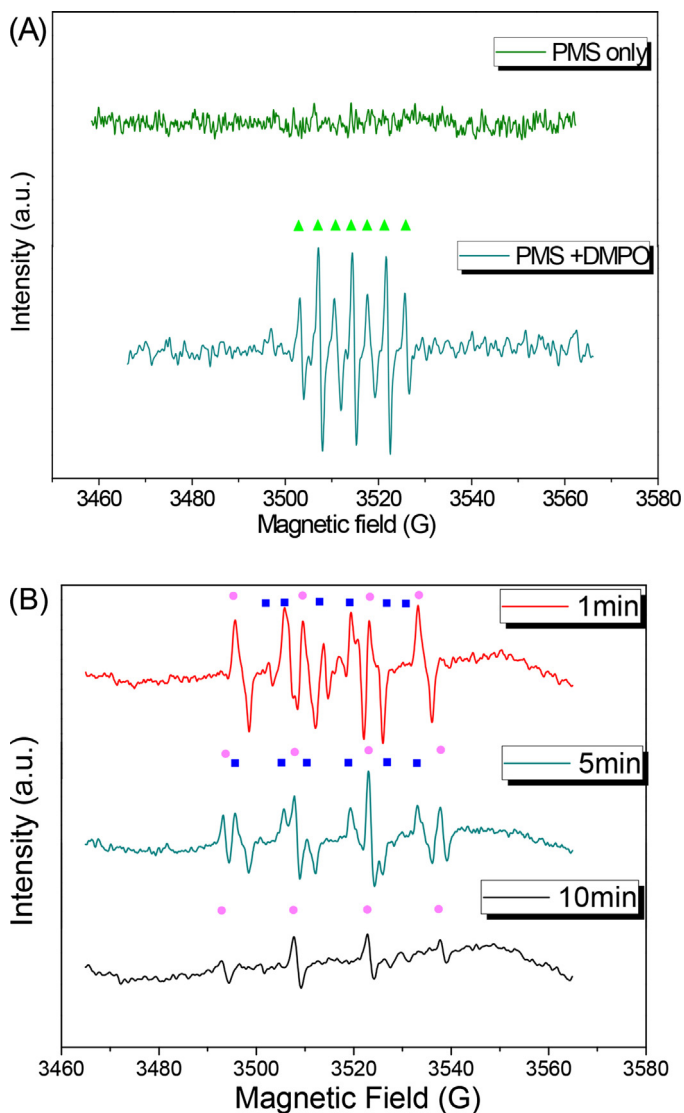


**Fig. 9.** EPR spectra in various conditions. Centerfield: 3510 G; sweep width: 100 G; microwave frequency: 9.87 GHz; modulation frequency: 100 GHz; and power: 18.11 mW. Reaction condition: phenol = 20 mg/L; catalyst loading = 0.2 g/L; Oxone® loading = 2.0 g/L, pH = 7.0; DMPO = 0.08 M. ▲: DMPOX; ●: DMPO-•OH; ■: DMPO-SO<sub>4</sub>•<sup>-</sup>.

Fig. 10 shows the relationship between phenol removal and the peak intensities of the DMPO-•OH/DMPO-SO<sub>4</sub>•<sup>-</sup> dependent on reaction time over Mn-100 catalyst. As shown clearly, at 1 min after addition of PMS, the DMPO-SO<sub>4</sub>•<sup>-</sup> reached the highest peak intensity. After that the intensity of DMPO-SO<sub>4</sub>•<sup>-</sup> gradually decreased, and reached zero at 10 min, indicating the complete consumption. However, the evolution of DMPO-•OH intensity had a different trend. It reached peak at 5 min and almost half of the intensity remained during the phenol degradation process. Combined the intensity variation of DMPO-•OH/DMPO-SO<sub>4</sub>•<sup>-</sup> with the phenol degradation profile, it could be induced that 80% of phenol degradation at the first 10 min might be ascribed to the dominant role of sulfate radicals.

To further investigate the major reactive species responsible for phenol degradation, classical quenching tests using ethanol (EtOH) and tert-butyl alcohol (TBA) as quenching agents were carried out. It was suggested that both EtOH and TBA could sufficiently quench •OH and the reaction rates are  $1.2 \times 10^9$ – $2.8 \times 10^9$  M<sup>-1</sup> s<sup>-1</sup> and  $3.8 \times 10^8$ – $7.6 \times 10^8$  M<sup>-1</sup> s<sup>-1</sup>, respectively [41]. SO<sub>4</sub>•<sup>-</sup> can be quenched more rapidly by the quenching agents with α-hydrogen. It was reported that the reaction rates of EtOH (with α-hydrogen) and TBA (without α-hydrogen) with SO<sub>4</sub>•<sup>-</sup> are  $1.6 \times 10^7$ – $7.7 \times 10^7$  and  $4.0 \times 10^5$ – $9.1 \times 10^5$  M<sup>-1</sup> s<sup>-1</sup>, respectively [41,42]. Therefore, by adding EtOH or TBA into the reaction solutions, the reactive radicals responsible for phenol degradation can be well differentiated.

Fig. 11 shows the results of the quenching tests in form of changes in reaction rate constant *k*. When 0.2 M EtOH was added in the original reaction solution, more than 20% of decrease in reaction rate was observed, compared with the original one, suggesting that part of the hydroxyl and sulfate radicals were quenched. However,

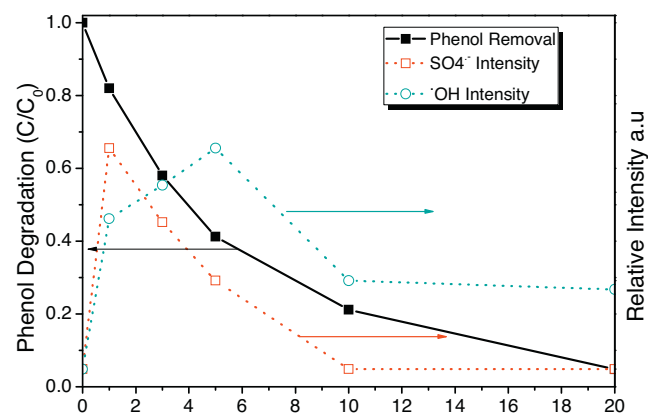


**Fig. 10.** Phenol removal profile and intensity variations of DMPO-•OH and DMPO-SO<sub>4</sub>•<sup>-</sup> during reaction on Mn-100.

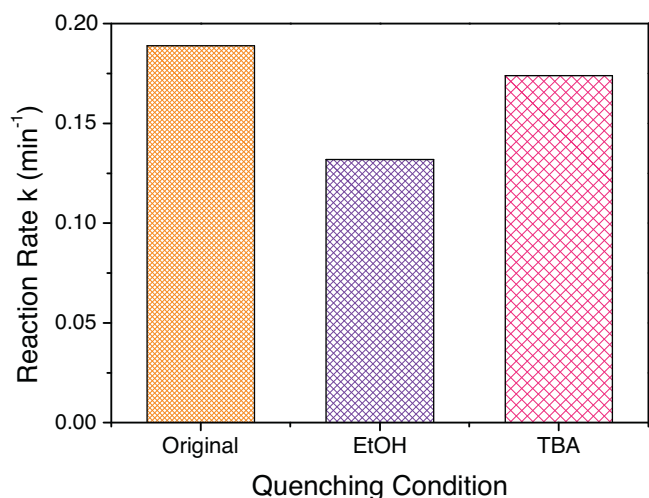
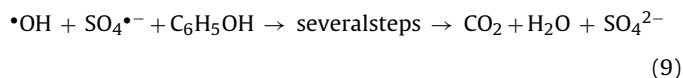
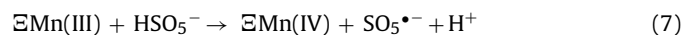
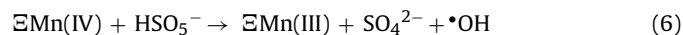
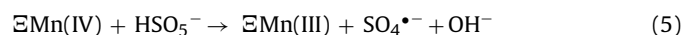


**Fig. 11.** Changes of reaction rate ( $k$ ) of catalysts with and without quenching agents of EtOH (0.2 M) and TBA (0.2 M). Reaction conditions: [phenol]<sub>0</sub> = 20 mg/L, catalyst loading = 0.2 g/L, Oxone® loading = 2.0 g/L, and  $T = 25^\circ\text{C}$ .

by addition of 0.2 M TBA, less than 5% decrease occurred to reaction rate. Therefore, since the addition of EtOH could incur more remarkable decrease in reaction rate than TBA, the dominant reactive species for phenol degradation were suggested to be sulfate radicals.

Based on EPR investigations as well as the results of the quenching tests, the mechanism of activation of PMS by  $\delta\text{-MnO}_2$  nanostructures for phenol degradation could be proposed as follows.



First,  $\delta\text{-MnO}_2$  activated PMS to generate  $\text{SO}_4^{\bullet-}$  and  $\bullet\text{OH}$  at the same time and thus Eqs. (5) and (6) happened simultaneously. Then most of the produced  $\text{SO}_4^{\bullet-}$  radicals were depleted quickly by reacting with phenol. During the reaction between  $\text{SO}_4^{\bullet-}$  radicals and phenol, some of the generated  $\bullet\text{OH}$  also participated, though at an inferior reaction rate (Eq. (9)). After the depletion of  $\text{SO}_4^{\bullet-}$ ,  $\bullet\text{OH}$  became the only reactive species to react with phenol. Meanwhile, the reduced  $\delta\text{-MnO}_2$  catalyst ( $\Xi\text{Mn(III)}$ ) reacted with PMS resulting in the recovery of the original  $\delta\text{-MnO}_2$  ( $\Xi\text{Mn(IV)}$ ) and the generation of  $\bullet\text{OH}$  (Eqs. (7) and (8)). Moreover, some of the competitive reactions also happened which might negatively influence the generation of the reactive radicals (Eqs. (10)–(12)).

#### 4. Conclusions

Shape-controlled 3D  $\text{MnO}_2$  hierarchical nanostructures were fabricated via a facile one-step hydrothermal method and their

catalytic activities in activation of PMS for phenol degradation were evaluated. Corolla-like  $\delta\text{-MnO}_2$ , prepared at a hydrothermal temperature of  $100^\circ\text{C}$ , showed 2D compact layers of nanosheets on the surface. It also had a higher catalytic activity than 3D sea-urchin like  $\alpha\text{-MnO}_2$ , which was prepared at  $110^\circ\text{C}$  and made of 1D tetragonal nanorods. Catalytic degradation of phenol was influenced by reaction temperature, the higher temperature would accelerate PMS activation to produce more radicals and thus enhance the reaction rates. The kinetic studies suggested that the heterogeneous catalytic system followed first-order kinetics and the activation energy was 25.3 kJ/mol. The catalyst stability tests revealed that corolla-like  $\delta\text{-MnO}_2$  possessed a high stability with little deactivation after several tests. The mechanism of catalytic reaction for PMS activation was investigated by EPR spectra and showed that both of  $\bullet\text{OH}$  and  $\text{SO}_4^{\bullet-}$  are produced in the activation processes, and  $\text{SO}_4^{\bullet-}$  plays a more critical role in phenol oxidation.

#### Acknowledgements

The authors acknowledge the use of equipment, scientific and technical assistance of the Curtin University Electron Microscope Facility and Centre for Microscopy Characterization, which has been partially funded by the University, State and Commonwealth Governments. H. S. thanks the support from Curtin Research Fellowship and Opening Project (KL13-02) of State Key Laboratory of Materials-Oriented Chemical Engineering, China.

#### References

- [1] A. Fortuny, J. Font, A. Fabregat, Appl. Catal. B 19 (1998) 165–173.
- [2] S. Esplugas, J. Gimenez, S. Contreras, E. Pascual, M. Rodriguez, Water Res. 36 (2002) 1034–1042.
- [3] M. Pera-Titus, V. Garcia-Molina, M.A. Banos, J. Gimenez, S. Esplugas, Appl. Catal. B 47 (2004) 219–256.
- [4] S. Wang, Dyes Pigm. 76 (2008) 714–720.
- [5] L. Hu, X. Yang, S. Dang, Appl. Catal. B 102 (2011) 19–26.
- [6] P. Shukla, H.Q. Sun, S.B. Wang, H.M. Ang, M.O. Tade, Catal. Today 175 (2011) 380–385.
- [7] P. Shukla, S.B. Wang, K. Singh, H.M. Ang, M.O. Tade, Appl. Catal. B 99 (2010) 163–169.
- [8] G.P. Anipsitakis, D.D. Dionysiou, Environ. Sci. Technol. 37 (2003) 4790–4797.
- [9] G.P. Anipsitakis, D.D. Dionysiou, Environ. Sci. Technol. 38 (2004) 3705–3712.
- [10] G.P. Anipsitakis, E. Stathatos, D.D. Dionysiou, J. Phys. Chem. B 109 (2005) 13052–13055.
- [11] X. Chen, J. Chen, X. Qiao, D. Wang, X. Cai, Appl. Catal. B 80 (2008) 116–121.
- [12] H.Q. Sun, S.Z. Liu, G.L. Zhou, H.M. Ang, M.O. Tade, S.B. Wang, ACS Appl. Mater. Interfaces 4 (2012) 5466–5471.
- [13] H.Q. Sun, G.L. Zhou, S.Z. Liu, H.M. Ang, M.O. Tade, S.B. Wang, ACS Appl. Mater. Interfaces 4 (2012) 6235–6241.
- [14] H.Q. Sun, H.W. Liang, G.L. Zhou, S.B. Wang, J. Coll. Interface Sci. 394 (2013) 394–400.
- [15] R. Watts, J. Sarasa, F. Loge, A. Teel, J. Environ. Engin. 131 (2005) 158–164.
- [16] L. Xu, C. Xu, M. Zhao, Y. Qiu, G.D. Sheng, Water Res. 42 (2008) 5038–5044.
- [17] H. Liang, H. Sun, A. Patel, P. Shukla, Z.H. Zhu, S. Wang, Appl. Catal. B 127 (2012) 330–335.
- [18] E. Saputra, S. Muhammad, H. Sun, A. Patel, P. Shukla, Z.H. Zhu, S. Wang, Catal. Commun. 26 (2012) 144–148.
- [19] E. Saputra, S. Muhammad, H. Sun, H.-M. Ang, M.O. Tade, S. Wang, Appl. Catal. B 142–143 (2013) 729–735.
- [20] H.Q. Sun, H.M. Ang, M.O. Tade, S.B. Wang, J. Mater. Chem. A 1 (2013) 14427–14442.
- [21] E. Saputra, S. Muhammad, H. Sun, H.-M. Ang, M.O. Tade, S. Wang, Appl. Catal. B 154–155 (2014) 246–251.
- [22] E. Saputra, S. Muhammad, H.Q. Sun, H.M. Ang, M.O. Tade, S.B. Wang, J. Coll. Interface Sci. 407 (2013) 467–473.
- [23] J.W. Long, C.P. Rhodes, A.L. Young, D.R. Rolison, Nano Lett. 3 (2003) 1155–1161.
- [24] C.R. Sides, C.R. Martin, Adv. Mater. 17 (2005) 125–128.
- [25] K.-H. Chang, C.-C. Hu, Appl. Phys. Lett. 88 (2006) 1931021–1931023.
- [26] Z. Li, Y. Ding, Y. Xiong, Y. Xie, Cryst. Growth Des. 5 (2005) 1953–1958.
- [27] P. Yu, X. Zhang, D. Wang, L. Wang, Y. Ma, Cryst. Growth Des. 9 (2008) 528–533.
- [28] X. Duan, J. Yang, H. Gao, J. Ma, L. Jiao, W. Zheng, CrystEngComm 14 (2012) 4196–4204.
- [29] W. Xiao, D. Wang, X.W. Lou, J. Phys. Chem. C 114 (2009) 1694–1700.
- [30] J.P. Hill, S. Alam, K. Ariga, C.E. Anson, A.K. Powell, Chem. Commun. (2008) 383–385.
- [31] P. Zhang, Y. Zhan, B. Cai, C. Hao, J. Wang, C. Liu, Z. Meng, Z. Yin, Q. Chen, Nano Res. 3 (2010) 235–243.



- [32] Y. Wang, H. Sun, H.M. Ang, M.O. Tadé, S. Wang, *Chem. Engin. J.* 245 (2014) 1–9.
- [33] E. Saputra, S. Muhammad, H. Sun, H.-M. Ang, M.O. Tadé, S. Wang, *J. Coll. Interface Sci.* 407 (2013) 467–473.
- [34] Y. Yao, Z. Yang, H. Sun, S. Wang, *Ind. Engin. Chem. Res.* 51 (2012) 14958–14965.
- [35] G.-D. Fang, D.D. Dionysiou, S.R. Al-Abed, D.-M. Zhou, *Appl. Catal. B* 129 (2013) 325–332.
- [36] Y. Yao, C. Xu, S. Yu, D. Zhang, S. Wang, *Ind. Engin. Chem. Res.* 52 (2013) 3637–3645.
- [37] H. Sun, Y. Wang, S. Liu, L. Ge, L. Wang, Z. Zhu, S. Wang, *Chem. Commun.* 49 (2013) 9914–9916.
- [38] L. Hu, F. Yang, W. Lu, Y. Hao, H. Yuan, *Appl. Catal. B* 134–135 (2013) 7–18.
- [39] G.M. Rosen, E.J. Rauckman, *Mol. Pharmacol.* 17 (1980) 233–238.
- [40] R.A. Floyd, L.M. Soong, *Biochem. Biophys. Res. Commun.* 74 (1977) 79–84.
- [41] G.V. Buxton, C.L. Greenstock, W.P. Helman, A.B. Ross, *J. Phys. Chem. Ref. Data* 17 (1988) 513–886.
- [42] P. Neta, R.E. Huie, A.B. Ross, *J. Phys. Chem. Ref. Data* 17 (1988) 1027–1284.